LETTER

doi:10.1038/nature13275

Uplift and seismicity driven by groundwater depletion in central California

Colin B. Amos[1], Pascal Audet[2], William C. Hammond[3], Roland Bürgmann[4,5], Ingrid A. Johanson[4] & Geoffrey Blewitt[3]

Groundwater use in California's San Joaquin Valley exceeds replenishment of the aquifer, leading to substantial diminution of this resource[1–4] and rapid subsidence of the valley floor[5]. The volume of groundwater lost over the past century and a half also represents a substantial reduction in mass and a large-scale unburdening of the lithosphere, with significant but unexplored potential impacts on crustal deformation and seismicity. Here we use vertical global positioning system measurements to show that a broad zone of rock uplift of up to 1–3 mm per year surrounds the southern San Joaquin Valley. The observed uplift matches well with predicted flexure from a simple elastic model of current rates of water-storage loss, most of which is caused by groundwater depletion[3]. The height of the adjacent central Coast Ranges and the Sierra Nevada is strongly seasonal and peaks during the dry late summer and autumn, out of phase with uplift of the valley floor during wetter months. Our results suggest that long-term and late-summer flexural uplift of the Coast Ranges reduce the effective normal stress resolved on the San Andreas Fault. This process brings the fault closer to failure, thereby providing a viable mechanism for observed seasonality in microseismicity at Parkfield[6] and potentially affecting long-term seismicity rates for fault systems adjacent to the valley. We also infer that the observed contemporary uplift of the southern Sierra Nevada previously attributed to tectonic or mantle-derived forces[7–10] is partly a consequence of human-caused groundwater depletion.

Hydrospheric mass changes exert direct influence over lithospheric deformation. Both seasonal and long-term changes to ice, snow or water loads may induce displacements of the Earth's surface[11–15] and can create stress perturbations that modulate activity on seismogenic faults[16–19]. A volume of groundwater approaching approximately 160 km^3 in California's Central Valley has been lost through pumping, irrigation and evapotranspiration over the past 150 years or so[3,4]. Historical and modern records demonstrate that groundwater depletion occurs primarily in the drier, hotter, southern portion of the basin[1,3] (the San Joaquin Valley), parallel to the central San Andreas Fault and adjacent to the high topography of the southern Sierra Nevada (Fig. 1). Previous studies demonstrating sensitivity to small-scale stress changes across this section of the San Andreas point to seasonal hydrologic[6] or temperature[20] variations to explain observed changes in seismicity rates[6] or strain in shallow boreholes[20].

Modest contemporary uplift rates of the southern Sierra Nevada observed using space geodesy[7–9] have been attributed to various tectonic and geomorphic drivers, such as buoyant response to mantle delamination[10], Basin and Range extensional faulting[21], and erosional mass transfer from Pleistocene glaciation[22]. Inferred stress change from epeirogenic uplift in the southern Sierra Nevada is also potentially linked to the transition from locked to creeping sections of the San Andreas Fault[23]. Here we seek to explore potential human impacts on contemporary deformation across this region through global positioning system (GPS) constraints on lithospheric flexure induced by anthropogenic groundwater level changes.

Continuous GPS networks spanning the southwestern USA provide a high-resolution framework for analysing crustal motion in three dimensions (Fig. 1). Longer available records and recently improved processing techniques enable determination of reliable GPS vertical velocities with a precision[24] of less than a millimetre per year, tied to the Earth system's centre of mass to within 0.5 mm yr^{-1} (refs 24 and 25). GPS station data were processed to create individual time series of vertical position and were then fitted with an empirical model including epoch position, velocity, and the amplitude and phase of annual and semiannual harmonic components (to model seasonal effects). This analysis includes only stations with at least two-and-a-half years of data and vertical rate uncertainties of $\leq$1.0 mm yr^{-1} (566 stations). Details of the GPS analysis and processing techniques are included in the Methods.

Figure 1 shows the distribution of vertical GPS rates across central California and east of the Sierra Nevada into the Great Basin. Long-term rates exclude GPS stations located within the San Joaquin Valley groundwater basin that display comparatively large signals owing to their position on soft sediment. These stations are affected by compaction-driven subsidence through loss of pore water[5], poro-elastic deformation related to groundwater level fluctuations[26], local irrigation and other processes unrelated to solid earth motion.

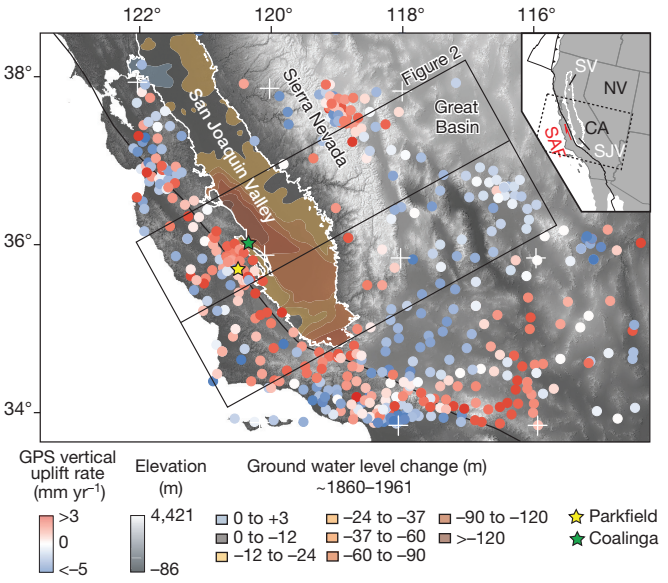

Figure 1 | Contemporary GPS vertical rates and groundwater decline. Map of vertical uplift rates from GPS stations (circles) spanning California and the western Great Basin. Stations in the valley showing anomalously larger signals and local irrigation effects are excluded. Contours show historical changes in the deep, confined aquifer[1]. The inset depicts the tectonic configuration of the Central Valley groundwater basin (SV, Sacramento Valley; SJV, San Joaquin Valley), and the San Andreas Fault (SAF).

[1]Geology Department, Western Washington University, Bellingham, Washington 98225-9080, USA. [2]Department of Earth Sciences, University of Ottawa, Ottawa, Ontario K1N 6N5, Canada. [3]Nevada Geodetic Laboratory, Nevada Bureau of Mines and Geology and Nevada Seismological Laboratory, University of Nevada, Reno, Nevada 89557, USA. [4]Berkeley Seismological Laboratory, University of California, Berkeley, California 94720-4760, USA. [5]Department of Earth and Planetary Science, University of California, Berkeley, California 97720-4767, USA.

©2014 Macmillan Publishers Limited. All rights reserved

Vertical rates across a transect from the central Coast Ranges to the relatively stable Great Basin range up to about 3 mm yr^{-1}. The highest average velocities concentrate along the margins of the valley (Fig. 2), near the locus of the greatest historical changes in the deep confined aquifer[1] (Fig. 1). The uplift rates of stations west of the San Joaquin Valley are more variable than those at bedrock sites in the Sierra Nevada, reflecting a higher proportion of stations on or near agricultural basins or active faults in the central Coast Ranges. Scatter in the vertical rate transect probably reflects shifts in the locus of groundwater change in comparison with historical averages[2], as well as some aleatory variability. Nearby earthquakes, such as the San Simeon rupture in 2003 of moment magnitude 6.5, may also influence stations near the coast with anomalously high rates near 2 mm yr^{-1} (Fig. 2). In the Sierra Nevada, the highest vertical rates occur along the western slope and steadily decay to the northeast in the Great Basin (Fig. 2). Previous studies show a similarly poor or inverse correlation between elevation and GPS uplift rates across the Sierra Nevada[7–9]. Modelling of postseismic viscoelastic relaxation following nearby historical earthquakes suggests that such transient strain accounts for only a fraction of the total observed vertical signal in the southern Sierra Nevada[9].

We compare vertical GPS rates with surface uplift predicted from an elastic half-space model simulating the response to load changes driven by variations in total water storage (Fig. 2) (see Methods). The model accounts for surface and subsurface deformation induced by line loads distributed across a 60-km-wide strip over the surface of an elastic half-space representing the San Joaquin Valley, the site of long-term, historical groundwater unloading. Using a range of elastic parameters, we fitted the GPS-derived vertical velocities with a rate of unloading of $8.8\ (\pm 1.3) \times 10^7$ N m^{-1} yr^{-1} (Fig. 2). We compare this estimate with the current average unloading rate in the valley based on changes in total water storage, measured using satellite gravimetry from the Gravity Recovery and Climate Experiment (GRACE) (ref. 3; see Methods). This change, measured between October 2003 and March 2010, yields an average equivalent unloading rate of $7.2\ (\pm 2.1) \times 10^7$ N m^{-1} yr^{-1}, slightly lower but in good overall agreement with the GPS-derived estimate.

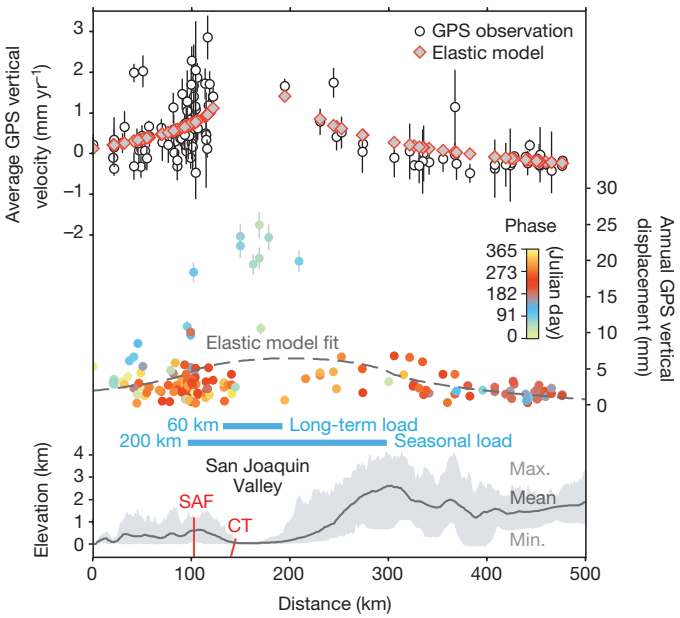

Figure 2 | GPS and model comparison. Swath profile of average contemporary vertical GPS velocity, annual GPS vertical displacement amplitude, and average topography from the central California Coast Range to the western Great Basin (SAF, San Andreas Fault; CT, Coalinga thrust). Vertical velocity and displacement amplitude are shown with 1σ uncertainties. The profile includes data from 121 stations and encompasses areas of the greatest historical and current change to groundwater levels (boxed in Fig. 1). The average GPS velocity is well fitted by an elastic model simulating surface uplift resulting from the decline in total water storage (including groundwater loss) centred along and parallel to the San Joaquin Valley. Seasonal changes in the annual GPS displacement (peak-to-peak amplitude) are distributed more broadly over the San Joaquin drainage basin, reflecting distribution of winter precipitation, snow load and reservoirs. Blue bars show the width of both the long-term and the seasonal loads used in the elastic model.

Assuming that changes in total water storage drive vertical motion surrounding the San Joaquin Valley, the GPS data reflect a combination of short-term, elastic response to ongoing groundwater depletion and longer-term viscous relaxation reflecting the history of hydrospheric mass changes. Slight overestimation of the unloading rate based on the GPS results leaves open the possibility of either a time-dependent (viscous) component of the uplift signal, or a (smaller) contribution of ongoing tectonic uplift. Both the overall match between the elastic model and observed GPS uplift (Fig. 2) and seasonal patterns inherent in the phase and amplitude of the GPS vertical time series, however, demonstrate the importance of the instantaneous (elastic) response to groundwater unloading.

Annual peak uplift for GPS stations in the Coast Ranges and Sierra Nevada occurs in the late summer and early autumn (Fig. 3), corresponding with diminished snow and surface water loads[27] and overlapping with the end of the summer growing season and peak groundwater pumping in the Central Valley (May to September; ref. 2). In contrast, recharge during the early spring drives larger-amplitude peak uplift within the valley through poro-elastic effects of aquifer water levels (Fig. 3 and ref. 2). Seasonal vertical displacements are more broadly distributed than average, long-term trends (Fig. 2), reflecting the variability in total water storage in upland catchments feeding the San Joaquin Valley. Notably, stations along the valley margins move upward annually in accordance with the Sierra Nevada and Coast Ranges during dry months and show a corresponding subsidence during the wet winter and spring (Fig. 3). These peripheral stations lead to the bimodal distribution for peak uplift times observed for the Central Valley (inset to Fig. 3), indicating that uplift from hydrospheric load changes dominates even the shortest-term signals in the vertical GPS measurements for stations unaffected by local irrigation or aquifer effects.

Flexure in the central Coast Ranges due to seasonal hydrospheric unloading in the San Joaquin Valley provides a viable mechanism to explain the annual modulation of seismicity on the San Andreas Fault. Both the locked and creeping fault sections at Parkfield (Fig. 1) exhibit an increase in the number of earthquakes greater than magnitude 1.25 during the late summer and autumn (Fig. 3), previously attributed to local changes in effective stress linked to the hydrologic cycle[6]. We explore the potential seasonal impacts of unloading and uplift of the Coast Ranges on short-term changes in the fault-normal stress resolved across the fault using the elastic half-space model (see Methods). Taking estimates of annual variations of 100–300 mm in equivalent water height in the San Joaquin Valley from GRACE data[3] and a wider load encompassing the Coast Ranges and the western Sierra Nevada, the elastic model produces between 3 mm and 8 mm of maximum annual vertical ground motion, in good agreement with the peak-to-peak amplitudes of annual uplift measured by GPS (Fig. 2). The corresponding fault-normal stress variations on the San Andreas Fault are near 1 kPa at seismogenic depths (Extended Data Fig. 4), with peak unclamping during the dry summer and autumn. Although we cannot rule out the potential feedback of reduced effective normal stress due to diffusion of pore fluids into fault zone rocks during recharge[6], our results suggest that unloading may contribute to seasonal modulation of seismic activity on the central San Andreas Fault. A similar mechanism was invoked to explain annual variations in seismicity in the Himalayas[18]. Stress changes due to groundwater unloading are somewhat higher for other historically active faults closer to the valley such as the Coalinga thrust system (Fig. 1), where peak-to-peak annual unloading gives rise to positive Coulomb stress changes of 1.0 kPa to 1.7 kPa (see Methods and Extended Data Fig. 4).

Given that relatively small annual stress perturbations (around 1 kPa) appear sufficient to modulate earthquakes along the central San Andreas Fault[6], we use the elastic model to estimate the stress rate caused by

©2014 Macmillan Publishers Limited. All rights reserved

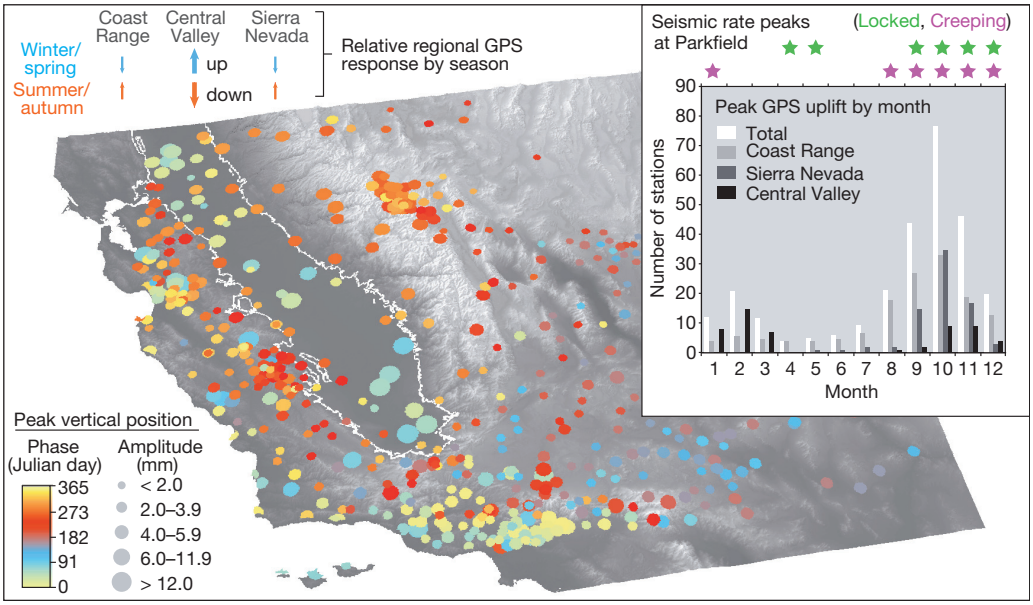

Figure 3 | Seasonal peak uplift from GPS. Phase and peak-to-peak amplitude of annual vertical GPS displacement for all stations included in our analysis. The inset shows histograms of peak uplift phase (binned by month) for stations in the San Joaquin Valley, Sierra Nevada, and Coast Range. Peaks in seismicity rate for the locked and creeping San Andreas Fault at Parkfield are defined as months with higher than average declustered seismicity[6]. Smaller-amplitude peak uplift in the Sierra Nevada and Coast Range during the dry summer and autumn is largely out of phase with larger-amplitude uplift in the San Joaquin Valley driven by the poro-elastic response to recharge during the wetter winter and spring. Stations peripheral to the valley show uplift patterns in accordance with nearby sites on bedrock, indicating the dominance of surface loads in driving vertical motions away from areas affected by local irrigation and groundwater fluctuations.

ongoing human-induced groundwater removal (see Methods). Taking an estimate of the unloading rate due to loss in water storage in the San Joaquin Valley of 8.8 ($\pm$1.3) $\times$ 10^7 N m^{-1} yr^{-1}, we calculate a rate of unclamping of 0.07–0.18 kPa yr^{-1} for the San Andreas Fault. Coulomb failure stress rates on the Coalinga thrusts are higher, averaging 0.13–0.57 kPa yr^{-1}. Estimates of total groundwater loss from historical and more recent water level records (around 160 km^3; refs 3 and 4) correspond to a reduction in the effective normal stress of 2.7–9.5 kPa for the San Andreas Fault, and a Coulomb stress change of 10–15 kPa at Coalinga, since the beginning of groundwater extraction in 1860. These results suggest that human activity may give rise to a gradual increase in the rate of earthquake occurrence, as suggested by earthquake catalogues in central California[6].

Future scenarios for groundwater in California suggest increasing demand for agricultural, urban and environmental use[2]. Climate change will probably exacerbate the stress on this resource through altered precipitation patterns, more frequent droughts, earlier snowmelt, larger floods, and increasing temperatures and evapotranspiration[28,29]. We demonstrate how long-term and seasonal hydrospheric mass changes due to groundwater removal significantly affect regional crustal deformation, which can lead to annual variations in small-earthquake frequency and longer-term changes of stresses on the San Andreas Fault. Our model explains recent vertical uplift rates previously attributed to epeirogenic deformation in central California[10], indicating that much of this signal results from anthropogenic groundwater removal. Taken together, our results highlight new and underappreciated links between human activity and solid earth processes driven by hydrospheric change.

METHODS SUMMARY

Elastic model. A two-dimensional model accounts for deformation from a normal line load distributed over a finite-width strip on the surface of the half-space[13,30]. The vertical displacement rate $\dot{u}$ at the surface ($z = 0$) along a profile perpendicular to the load centred at $x = x_d$ is given by:

$$\dot{u}(x,z=0) = \frac{(1-\nu)\dot{N}_0}{\pi G(2a)}[2a + (x-x_d-a)\ln|x-x_d-a| - (x-x_d+a)\ln|x-x_d+a|] + K$$

where x and z are the horizontal and vertical dimensions, respectively, $\dot{N}_0$ is the rate of line load, ν is Poisson's ratio, G is the shear modulus, a is the strip half-width and K is a far-field rate offset correction. The load is centred on the middle of the valley and covers its entire width ($2a$ = 60 km). Given a range of elastic parameters (ν = 0.25, G = 35 $\pm$ 5 GPa), we fit observed vertical velocities using a line-load rate with $\dot{N}_0$ = 8.8 ($\pm$1.3) $\times$ 10^7 N m^{-1} yr^{-1} (Fig. 2).

Unloading from groundwater loss. The Sacramento and San Joaquin basins lost an estimated volume of 30.9 ($\pm$2.6) km^3 in total water storage between October 2003 and March 2010 (ref. 3). Total water storage change in the San Joaquin Valley (21.5 $\pm$ 6.2 km^3) equates to an unloading of 3.3 ($\pm$1.0) $\times$ 10^{13} N yr^{-1} over a valley length of 450 km, giving an equivalent line load of $\dot{N}_0$ = 7.2 ($\pm$2.1) $\times$ 10^7 N m^{-1} yr^{-1}, in agreement with the elastic model.

Unclamping of the San Andreas Fault. The unclamping rate (change in fault normal stress) on a vertical fault is calculated as[30]:

$$\dot{\tau}_{xx} = \frac{\dot{N}_0}{2\pi a}[(\theta_1-\theta_2) + \sin(\theta_1-\theta_2)\cos(\theta_1+\theta_2)]$$

where θ_1 and θ_2 are the angles from the load edges to any point at depth, measured clockwise from the positive x direction. For the San Andreas Fault, located about 70 km from the 60-km-wide load centre, we estimate an unclamping rate of 0.07–0.18 kPa yr^{-1} at seismogenic depths (5–15 km) from groundwater unloading.

Online Content Any additional Methods, Extended Data display items and Source Data are available in the online version of the paper; references unique to these sections appear only in the online paper.

Received 24 October 2013; accepted 30 March 2014.
Published online 14 May 2014.

1. Williamson, A. K., Prudic, D. E. & Swain, L. A. Ground-water flow in the Central Valley, California. *US Geol. Surv. Prof. Pap.* 1401-D (1989).
2. Faunt, C. C. (ed.) Groundwater availability of the Central Valley aquifer, California. *US Geol. Surv. Prof. Pap.* 1766 (2009).
3. Famiglietti, J. S. *et al.* Satellites measure recent rates of groundwater depletion in California's Central Valley. *Geophys. Res. Lett.* **38,** L03403 (2011).
4. Scanlon, B. R. *et al.* Groundwater depletion and sustainability of irrigation in the US High Plains and Central Valley. *Proc. Natl Acad. Sci. USA* **109,** 9320–9325 (2012).
5. Poland, J. F., Lofgren, B. E., Ireland, R. L. & Pugh, R. G. Land subsidence in the San Joaquin Valley, California, as of 1972. *US Geol. Surv. Prof. Pap.* 437-H (1975).
6. Christiansen, L. B., Hurwitz, S. & Ingebritsen, S. E. Annual modulation of seismicity along the San Andreas Fault near Parkfield, CA. *Geophys. Res. Lett.* **34,** L04306 (2007).

©2014 Macmillan Publishers Limited. All rights reserved

7. Fay, N. P., Bennett, R. A. & Hreinsdóttir, S. Contemporary vertical velocity of the central Basin and Range and uplift of the southern Sierra Nevada. *Geophys. Res. Lett.* **35,** L20309 (2008).
8. Bennett, R. A., Fay, N. P., Hreinsdóttir, S., Chase, C. & Zandt, G. Increasing long-wavelength relief across the southeastern flank of the Sierra Nevada, California. *Earth Planet. Sci. Lett.* **287,** 255–264 (2009).
9. Hammond, W. C., Blewitt, G., Li, Z., Plag, H. P. & Kreemer, C. Contemporary uplift of the Sierra Nevada, western United States, from GPS and InSAR measurements. *Geology* **40,** 667–670 (2012).
10. Saleeby, J., Saleeby, Z. & Le Pourhiet, L. Epeirogenic transients related to mantle lithosphere removal in the southern Sierra Nevada region, California: Part II. Implications of rock uplift and basin subsidence relations. *Geosphere* **9,** 394–425 (2013).
11. Holzer, T. L. Elastic expansion of the lithosphere caused by groundwater depletion. *J. Geophys. Res.* **84,** 4689–4698 (1979).
12. van Dam, T. *et al.* Crustal displacements due to continental water loading. *Geophys. Res. Lett.* **28,** 651–654 (2001).
13. Jiang, Y., Dixon, T. H. & Wdowinski, S. Accelerating uplift in the North Atlantic region as an indicator of ice loss. *Nature Geosci.* **3,** 404–407 (2010).
14. Nof, R. N. *et al.* Rising of the lowest place on Earth due to Dead Sea water-level drop: evidence from SAR interferometry and GPS. *J. Geophys. Res.* **117,** B05412 (2012).
15. Fu, Y. & Freymueller, J. T. Seasonal and long-term vertical deformation in the Nepal Himalaya constrained by GPS and GRACE measurements. *J. Geophys. Res.* **117,** B03407 (2012).
16. Heki, K. Snow load and seasonal variation of earthquake occurrence in Japan. *Earth Planet. Sci. Lett.* **207,** 159–164 (2003).
17. Luttrell, K., Sandwell, D., Smith-Konter, B., Bills, B. & Bock, Y. Modulation of the earthquake cycle at the southern San Andreas fault by lake loading. *J. Geophys. Res.* **112,** B08411 (2007).
18. Bettinelli, P. *et al.* Seasonal variations of seismicity and geodetic strain in the Himalaya induced by surface hydrology. *Earth Planet. Sci. Lett.* **266,** 332–344 (2008).
19. González, P. J., Tiampo, K. F., Palano, M., Cannavó, F. & Fernández, J. The 2011 Lorca earthquake slip distribution controlled by groundwater crustal unloading. *Nature Geosci.* **5,** 821–825 (2012).
20. Ben-Zion, Y. & Allam, A. A. Seasonal thermoelastic strain and postseismic effects in Parkfield borehole dilatometers. *Earth Planet. Sci. Lett.* **379,** 120–126 (2013).
21. Christensen, M. N. Late Cenozoic crustal movements in the Sierra Nevada of California. *Geol. Soc. Am. Bull.* **77,** 163–182 (1966).
22. Small, E. E. & Anderson, R. S. Geomorphically driven late Cenozoic rock uplift in the Sierra Nevada, California. *Science* **270,** 277–281 (1995).
23. Le Pourhiet, L. & Saleeby, J. Lithospheric convective instability could induce creep along part of the San Andreas fault. *Geology* **41,** 999–1002 (2013).
24. Blewitt, G., Kreemer, C., Hammond, W. C. & Goldfarb, J. M. Terrestrial reference frame NA12 for crustal deformation studies in North America. *J. Geodyn.* **72,** 11–24 (2013).
25. Altamimi, Z., Collilieux, X. & Métivier, L. ITRF2008: an improved solution of the international terrestrial reference frame. *J. Geod.* **85,** 457–473 (2011).
26. Schmidt, D. A. & Bürgmann, R. Time-dependent land uplift and subsidence in the Santa Clara valley, California, from a large interferometric synthetic aperture radar data set. *J. Geophys. Res.* **108,** 2416 (2003).
27. Argus, D., Fu, Y. & Landerer, F. Seasonal variation in total water storage in California inferred from GPS observations of vertical land motion. *Geophys. Res. Lett.* **41,** 1971–1980 (2014).
28. Dettinger, M. D. & Cayan, D. R. Large-scale atmospheric forcing of recent trends toward early snowmelt runoff in California. *J. Clim.* **8,** 606–623 (1995).
29. California Department of Water Resources. California water plan update 2005. Volume 1: Strategic Plan. *Dep. Water Res. Bull.* 160–05 (2005).
30. Jeager, J., Cook, N. & Zimmerman, R. *Fundamentals of Rock Mechanics* 4th edn (Blackwell, 2007).

Acknowledgements Funding for this work comes from NSF EarthScope award number EAR-1252210 to G.B. and W.C.H. GPS data were collected using the EarthScope Plate Boundary Observatory, SCIGN, BARGEN, BARD, CORS and IGS networks. We are particularly grateful to UNAVCO for operating the vast majority of GPS stations used in this project. GPS data were processed using the GIPSY OASIS II software and data products from the Jet Propulsion Laboratory.

Author Contributions C.B.A. and P.A. performed the analysis and wrote the paper. W.C.H. and G.B. analysed and processed the GPS data. All authors contributed to the interpretations and preparation of the final manuscript.

Author Information Reprints and permissions information is available at www.nature.com/reprints. The authors declare no competing financial interests. Readers are welcome to comment on the online version of the paper. Correspondence and requests for materials should be addressed to C.B.A. (colin.amos@wwu.edu).

©2014 Macmillan Publishers Limited. All rights reserved

METHODS

GPS data processing. We use data from continuously recording GPS stations between −122° and −114° longitude and 34° to 38° latitude that had time series longer than 2.5 years that were >50% complete (Extended Data Fig. 1). This data set includes 566 continuous GPS stations within this geographic region. No episodic campaign or semi-continuous stations were included. Percentage completeness is defined as the number of daily solutions for the station divided by the number of potential daily solutions given the duration of the time series. Larger values for percentage completeness are preferred in order to best resolve seasonal oscillations of position.

The data were processed as a part of a >11,000 station mega-network analysis system that retrieves data daily and updates solutions weekly. We use the GIPSY/OASIS software provided by the Jet Propulsion Laboratory to estimate station coordinates every 24 h using the Precise Point Positioning method[31]. Ionosphere-free combinations of carrier phase and pseudorange were obtained every 5 min. Calibrations were applied for all antennas, ground receivers and satellite transmitters. To model tropospheric refractivity, the Global Mapping Function was applied[32], with tropospheric wet zenith delay and horizontal gradients estimated as stochastic random-walk parameters every 5 min (ref. 33). The observable model includes ocean tidal loading (including companion tides) coefficients supplied by Chalmers University[34]. Ambiguity resolution was applied to double differences of the estimated one-way bias parameters[35], using the wide lane and phase bias method, which phase-connects individual stations to IGS stations in common view[36]. Satellite orbit and clock parameters were provided by the Jet Propulsion Laboratory, who determine these parameters in a global fiducial-free analysis using a subset of the available IGS core stations as tracking sites. Output station coordinates are initially in the loose frame of the Jet Propulsion Laboratory's fiducial-free GPS orbits. These were transformed into reference frame IGS08 using daily seven-parameter transformations supplied by the Jet Propulsion Laboratory. IGS08 is derived from ITRF2008 (ref. 37) and consists of 232 globally distributed IGS stations[38]. Finally, the solutions are aligned with our custom reference frame (NA12) that co-rotates with stable North America[24]. This alignment is applied to each daily solution and provides a spatial filter to suppress errors correlated at the continental scale. The mean formal uncertainty in daily vertical coordinate is <3.0 mm. A summary reference table for GPS solution methodology is given at http://geodesy.unr.edu/gps/ngl.acn.The resulting time series are used to estimate rates of motion with respect to stable North America.

GPS time series analysis. An outlier exclusion criterion was applied to remove daily solutions that were more than 20 mm from the expected position based on a provisional time series model, or having position uncertainty greater than 20 mm. For each of the three components (east, north, up) of each GPS time series we solved for the intercept b, rate v, steps at the times t_{eqp} of N known equipment changes that can introduce discontinuities of size D. We solve for annual and semiannual seasonal terms by solving for the cosine (C_i) and sine (S_i) terms. For example, the east component is:

$$e(t) = b + vt + \sum_{i=1}^{N} D_i \mathcal{H}(t - t_{\mathrm{eqp},i}) + \sum_{k=1}^{2} [C_k \cos(2\pi k t) + S_k \sin(2\pi k t)]$$

where $\mathcal{H}(t)$ is the Heaviside step function, where t is in years. We use a damped linear inversion with weights on the prior uncertainties of the model parameters scaled to allow the expected range of values for each parameter. However, because only continuously recording GPS stations were used, all parameters in the estimation (including seasonal terms) were well constrained, so the damping parameters had little influence on the solutions. The amplitude of the annual terms were calculated with:

$$A = \sqrt{(C^2 + S^2)}$$

and the day of year from:

$$\mathrm{day} = \left(\frac{365}{2\pi}\right) \tan^{-1}\left(\frac{S}{C}\right)$$

Finally, stations were excluded if their rate uncertainty was greater than 1 mm yr^{-1} or their rate was clearly anomalous (that is, greater than 100 mm yr^{-1}). In all, we estimated solutions for 566 stations, 96% of which have time series duration greater than 4.0 years, and 92% of which are 80% or more complete (Extended Data Fig. 2). Example vertical GPS time series are shown in Extended Data Fig. 3. GPS time series parameters, including vertical uplift rate and the amplitude and timing of peak uplift are included as source data for Fig. 1.

Elastic half-space model. We use an elastic half-space model for calculating the elastic response of the crust to changes in total water storage. The model is two-dimensional and accounts for surface and subsurface deformation induced by a line load over the surface of the half-space along a finite-width strip (half-width a, Extended Data Fig. 4a). Model derivation can be found in ref. 30, with a small correction from ref. 13. The normal displacement of the surface ($z = 0$) along a profile perpendicular to the load centred at $x = x_d$ is given by

$$u(x, z=0) = \frac{(1-\nu)N_0}{\pi G(2a)} [2a + (x - x_\mathrm{d} - a)\ln|x - x_\mathrm{d} - a| - (x - x_\mathrm{d} + a)\ln|x - x_\mathrm{d} + a|] + K$$

where x and z are the horizontal and vertical dimensions, respectively, N_0 is a line load, ν is Poisson's ratio, G is the shear modulus, a is the strip half-width and K is a far-field rate offset correction. We fix the position of the line load to the centre of the San Joaquin Valley, and use a load width of $2a = 60$ km corresponding to the average width of the valley floor. Given a range of elastic parameters ($\nu = 0.25$, $G = 35 \pm 5$ GPa), we can fit the vertical velocities derived from the GPS data by a line-load rate with $\dot{N}_0 = 8.8\ (\pm 1.3) \times 10^7$ N m^{-1} yr^{-1} (see Fig. 2). Goodness of fit is estimated using a reduced chi-square criterion. Our best-fit model has a reduced chi-square of 1.9, indicating a reasonably good fit.

Unloading from estimated mass loss. The combined Sacramento–San Joaquin River basins lost an estimated volume of 30.9 (± 2.6) km^3 in total water storage over a 6.5-year period between October 2003 and March 2010 (ref. 3). Of this volume, 20.3 (± 3.8) km^3 is attributed to loss of groundwater in the Central Valley, 80% of which occurred in the San Joaquin Valley. Assuming that changes in total water storage not related to groundwater (for example, soil moisture, surface water and snow) are distributed equally between the Sacramento and San Joaquin basins, the total water storage change in the San Joaquin Valley over the 6.5-year period is 21.5 (± 6.2) km^3. This change is equivalent to a rate of mass loss of 3.3 (± 1.0) $\times 10^3$ gigatons per year, and therefore a rate of unloading of 3.2 (± 1.0) $\times 10^{13}$ N yr^{-1} distributed over the 450 km length of the valley. Taking into account the range of uncertainties in groundwater and total water storage change[3], the equivalent line-load rate is thus $\dot{N}_0 = 7.2\ (\pm 2.1) \times 10^7$ N m^{-1} yr^{-1}, in agreement with the estimate from the elastic model based on the vertical GPS velocities. If we add the estimated 1860–2003 depletion of 140 km^3 (ref. 4) to the 2003–2010 water loss, the cumulative historic load decrease amounts to $\sim 3.5 \times 10^9$ N m^{-1}.

Stress modelling. The two-dimensional stress components at any point at depth caused by a distributed line load N_0 (in N m^{-1}, the negative value indicates unloading) at the surface of the elastic half-space are calculated as[30]:

$$\tau_{xx} = \frac{N_0}{2\pi a}[(\theta_1 - \theta_2) + \sin(\theta_1 - \theta_2)\cos(\theta_1 + \theta_2)]$$

$$\tau_{zz} = \frac{N_0}{2\pi a}[(\theta_1 - \theta_2) - \sin(\theta_1 - \theta_2)\cos(\theta_1 + \theta_2)]$$

$$\tau_{xz} = \frac{N_0}{2\pi a}[\sin(\theta_1 - \theta_2)\sin(\theta_1 + \theta_2)]$$

where θ_1 and θ_2 are the angles from both edges of the load measured clockwise from the positive x direction, a is the load half-width and z is positive downward (Extended Data Fig. 4a). The shear and normal stress components resolved on a fault plane dipping at an angle φ with a strike direction normal to the xz plane are given by:

$$\tau_\mathrm{n} = \tau_{zz}\cos^2(\varphi) - 2\tau_{xz}\sin(\varphi)\cos(\varphi) + \tau_{xx}\sin^2(\varphi)$$

$$\tau_\mathrm{z} = (\tau_{zz} - \tau_{xx})\sin(\varphi)\cos(\varphi) + \tau_{xz}(\cos^2(\varphi) - \sin^2(\varphi))$$

Using Coulomb failure assumptions[30], the Coulomb failure stress is expressed as:

$$\sigma_\mathrm{c} = |\tau_\mathrm{z}| + \mu(\tau_\mathrm{n} - p) + S$$

where μ is the coefficient of friction, p is pore-fluid pressure and S is cohesion. Assuming that p, S and μ are constant over time, the change in Coulomb stress is given by[39]:

$$\Delta\sigma_\mathrm{c} = \Delta|\tau_\mathrm{z}| + \mu\Delta\tau_\mathrm{n}$$

where $\Delta\tau_\mathrm{n}$ is positive for tension[30,39]. Similarly, the Coulomb stressing rate is given by:

$$\dot{\sigma}_\mathrm{c} = |\dot{\tau}_\mathrm{z}| + \mu\dot{\tau}_\mathrm{n}$$

The first term on the right-hand side is valid for an isotropic failure plane. We consider the change in shear stress in the slip direction (or rake) and vary the sign

©2014 Macmillan Publishers Limited. All rights reserved

of the change in shear stress accordingly. For the San Andreas Fault we consider a dip angle of 90° and the unclamping stress (or stress rate) is given simply by $\Delta\tau_{xx}$ (or $\dot{\tau}_{xx}$). For the Coalinga blind thrust we use dip angles ranging between 15° and 30° (refs 40 and 41) and a negative change in shear stress. We also consider a 65° northeast-dipping fault with a positive slip direction, simulating stress conditions on the Nuñez thrust fault. For each fault we calculate the normal and shear stress components at depths of 5 km and 15 km, representative of the seismogenic depth in Central California.

Rate of unclamping of the San Andreas Fault. The rate of unclamping on a vertical fault (change in fault normal stress) can be calculated as[30]:

$$\dot{\tau}_{xx} = \frac{\dot{N}_0}{2\pi a}\left[(\theta_1 - \theta_2) + \sin(\theta_1 - \theta_2)\cos(\theta_1 + \theta_2)\right]$$

where θ_1 and θ_2 are the angles from both edges of the loading strip to any point at depth, measured clockwise from the positive x direction. Taking an estimate of the unloading rate due to loss in water storage of $8.8\ (\pm 1.3) \times 10^7\ \mathrm{N\,m^{-1}\,yr^{-1}}$, as well as average spatial parameters for the San Andreas Fault (load width of $2a = 60$ km; distance to centre of the distributed line load of around 70 km; seismogenic depths of 5–15 km), we estimate a rate of unclamping of 0.07–0.18 kPa $\mathrm{yr^{-1}}$ at the seismogenic depth along the San Andreas Fault due to the elastic rebound caused by unloading (Extended Data Fig. 4b and c).

For the Coalinga blind thrust, we calculate the normal (τ_n) and shear (τ_s) stress rates resolved on a range of fault planes and depths. The Coulomb failure stress rate (ignoring pore pressure), $\dot{\sigma}_c = |\dot{\tau}_z| + \mu\dot{\tau}_n$ (ref. 30), is then calculated with $\mu = 0.7$.

Seasonal vertical displacements and stress changes. The elastic model can be used to estimate total vertical displacements caused by variations in total water storage. The model considered is more broadly distributed over the Coast Range, the San Joaquin Valley and the western Sierra Nevada (width of 200 km; Fig. 2), corresponding to the approximate total width of the San Joaquin River drainage basin. Taking an average of 200 mm of change in total water storage, we estimate a load of $\sim 4 \times 10^8\ \mathrm{N\,m^{-1}}$, which produces annual vertical displacements of 3–8 mm within the load extent (Fig. 2). The associated stress variations on the San Andreas Fault are about 1 kPa and the Coulomb stress changes on the Coalinga thrust are 1.0–1.7 kPa (Extended Data Fig. 4d and e). Varying the width of the distributed line loads by ±20 km and the load centre by ±10 km has only a small impact (<0.5 kPa) on the resolved seasonal stress changes on the faults.

31. Zumberge, J. F., Heflin, M. B., Jefferson, D. C., Watkins, M. M. & Webb, F. H. Precise point positioning for the efficient and robust analysis of GPS data from large networks. *J. Geophys. Res.* **102,** 5005–5017 (1997).
32. Boehm, J., Niell, A., Tregoning, P. & Schuh, H. Global mapping function (GMF): a new empirical mapping function based on numerical weather model data. *Geophys. Res. Lett.* **33,** L07304 (2006).
33. Bar-Sever, Y. E., Kroger, P. M. & Borjesson, J. A. Estimating horizontal gradients of tropospheric path delay with a single GPS receiver. *J. Geophys. Res.* **103,** 5019–5035 (1998).
34. Scherneck, H.-G. A parametrized solid earth tide model and ocean tide loading effects for global geodetic baseline measurements. *Geophys. J. Int.* **106,** 677–694 (1991).
35. Blewitt, G. Carrier phase ambiguity resolution for the Global Positioning System applied to geodetic baselines up to 2000 km. *J. Geophys. Res.* **94,** 10187–10283 (1989).
36. Bertiger, W. *et al.* Single receiver phase ambiguity resolution with GPS data. *J. Geod.* **84,** 327–337 (2010).
37. Altamimi, Z., Collilieux, X. & Métivier, L. ITRF2008: an improved solution of the international terrestrial reference frame. *J. Geodesy* **85,** 457–473 (2011).
38. Rebischung, P. *et al.* IGS08: The IGS realization of ITRF2008. *GPS Solut.* **16,** 483–494 (2012).
39. Harris, R. A. Stress triggers, stress shadows, and implications for seismic hazard. *J. Geophys. Res.* **103,** 24347–24358 (1998).
40. Stein, R. S. & Ekstrom, G. E. Seismicity and geometry of a 110-km long blind thrust fault. 2. Synthesis of the 1982-1985 California earthquake sequence. *J. Geophys. Res.* **97,** 4865–4883 (1992).
41. Toda, S. & Stein, R. S. Response of the San Andreas fault to the 1983 Coalinga-Nuñez earthquakes: an application of interaction-based probabilities. *J. Geophys. Res.* **107,** 2126 (2002).

©2014 Macmillan Publishers Limited. All rights reserved

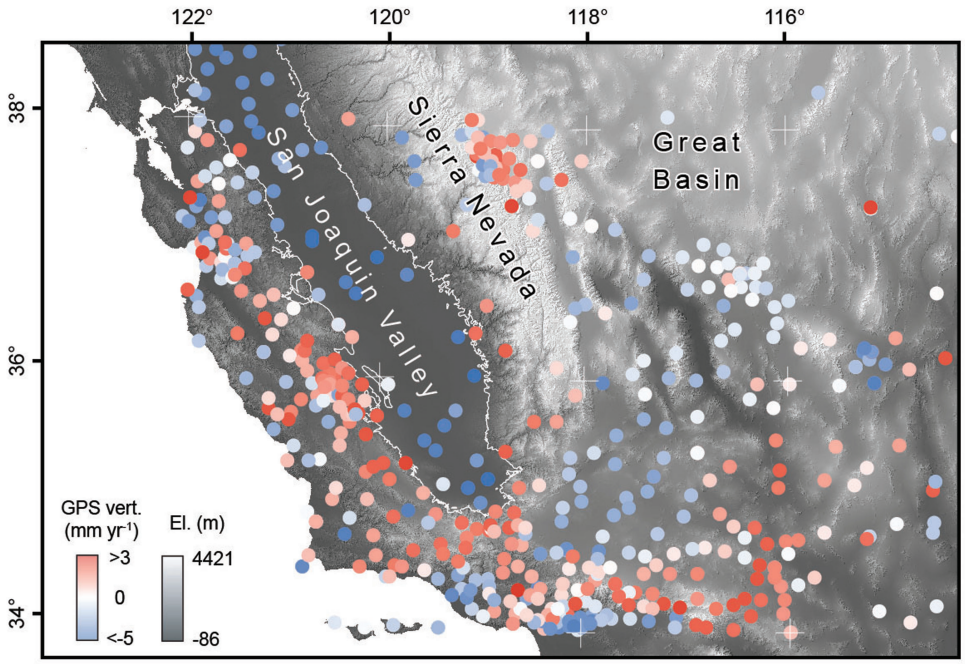

Extended Data Figure 1 | Vertical GPS data. Map of vertical uplift rates spanning California and the western Great Basin, including stations within the Central Valley groundwater basin. El., elevation; GPS vert., GPS vertical velocity.

©2014 Macmillan Publishers Limited. All rights reserved

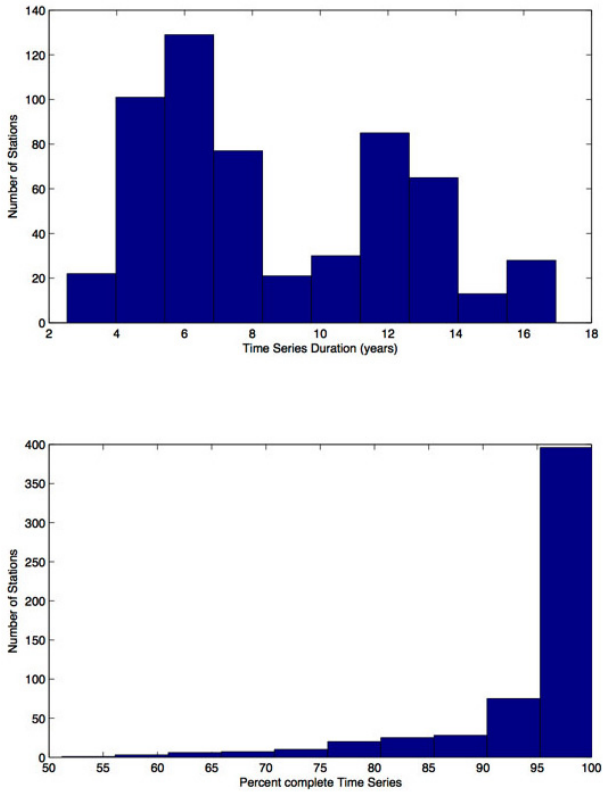

Extended Data Figure 2 | GPS time series. The top panel shows a histogram of the duration of GPS time series. 96% are longer than 4.0 years. The bottom panel shows a histogram of the percentage of complete time series. 92% are greater than 80% complete.

©2014 Macmillan Publishers Limited. All rights reserved

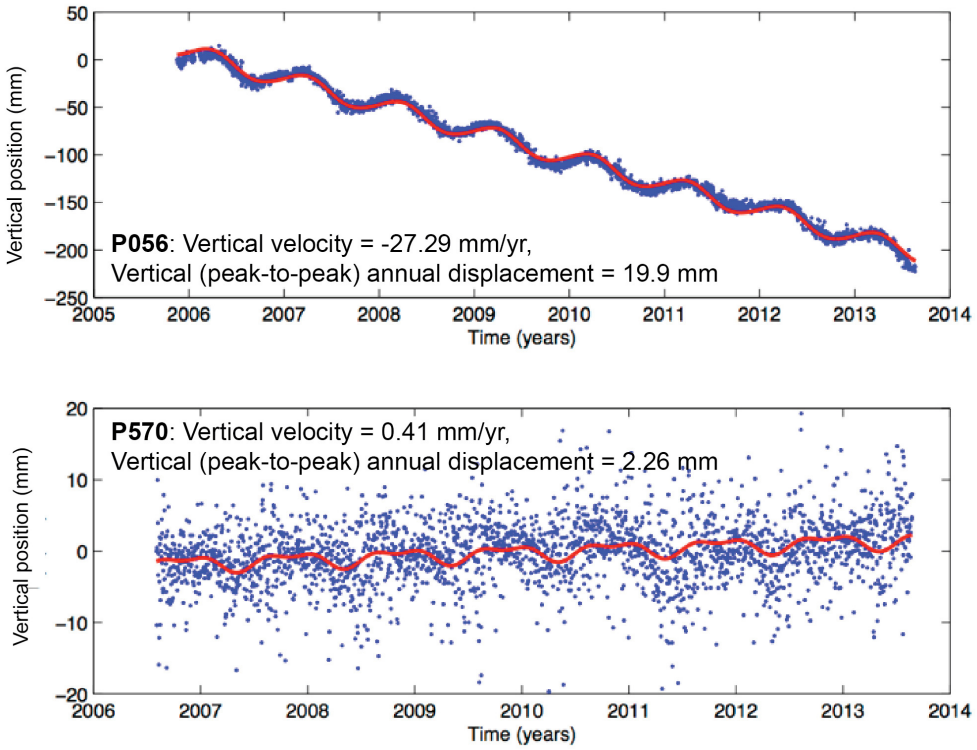

Extended Data Figure 3 | GPS time series. Example vertical GPS time series for stations P056 and P570. Blue dots are daily vertical position solutions, red lines are the model estimated to represent the time series. The station P056 is in the southern Central Valley near Porterville, California. The station P570 is near Weldon, California, east of Lake Isabella.

©2014 Macmillan Publishers Limited. All rights reserved

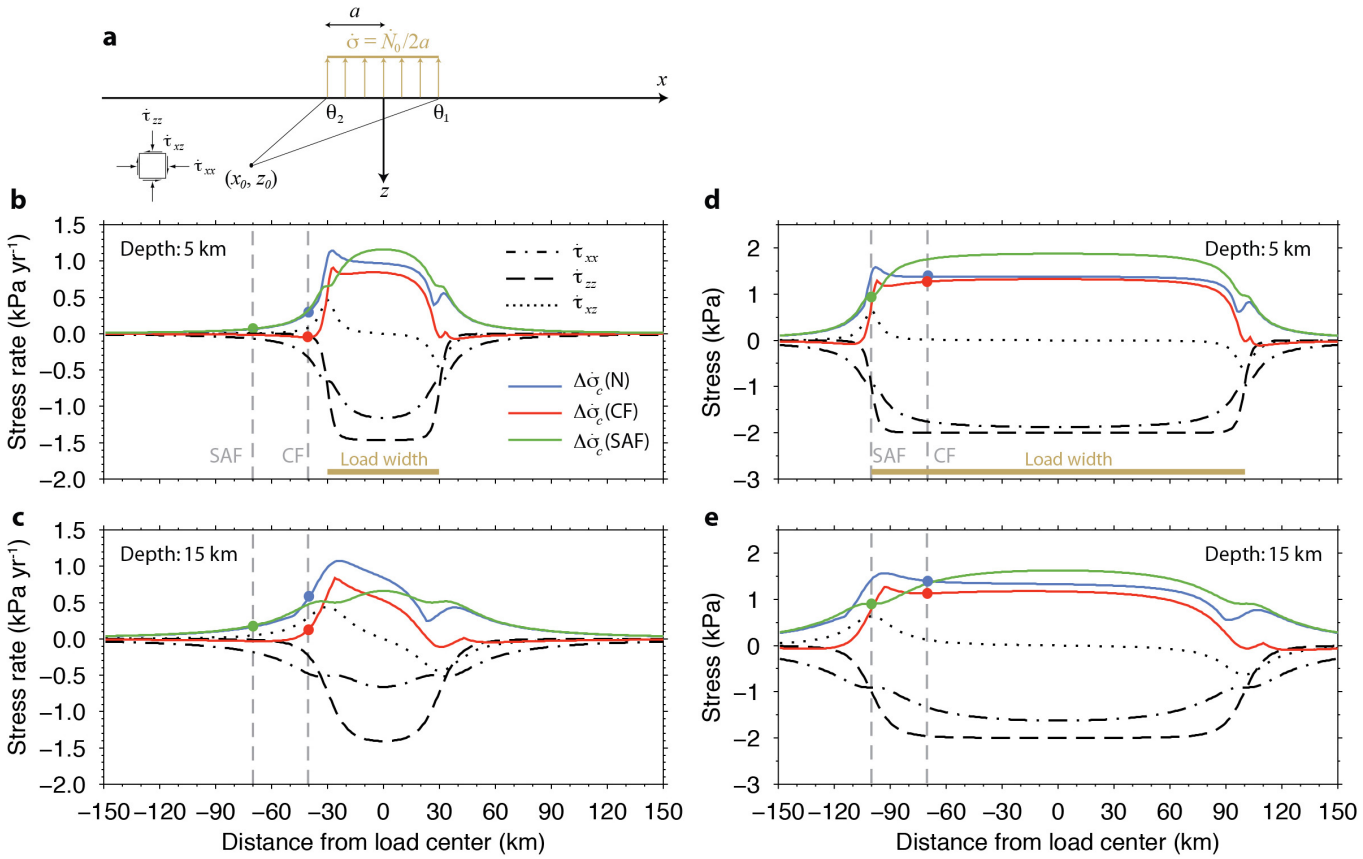

Extended Data Figure 4 | Stress profiles from distributed line loads of an elastic half-space. **a**, Model setup, where $\dot{N}_0$ is the line-load rate, a is the load half-width, and θ_1 and θ_2 measure the angle downward from the positive x axis to any point (x_0, z_0) at depth. $\dot{\tau}$ and $\Delta\dot{\sigma}_c$ give the stress rates and Coulomb stress rates, respectively. **b**, **c**, Stress rates at depths of 5 km (**b**) and 15 km (**c**) calculated from the long-term rate of unloading over the San Joaquin Valley with $a = 30$ km. Vertical dashed lines labelled SAF and CF represent the locations of the San Andreas Fault and the Coalinga blind thrust faults (including the Nuñez fault), respectively, relative to the load centre. Black and coloured lines indicate stress components and Coulomb stress changes, respectively. The blue curves labelled N show Coulomb stress calculations for favourably oriented faults with a 65° dip, representing the Nuñez fault. For the red curve representing the Coalinga fault (CF), the calculations are performed using a dip of 30° for unfavourably oriented faults. The green curve represents unclamping stress for vertically dipping faults such as the San Andreas Fault. **d**, **e**, Stress changes at depths of 5 km and 15 km from seasonal (peak-to-peak) load changes over the San Joaquin River Basin with $a = 100$ km (full width of 200 km). The position of the San Andreas Fault and Coalinga faults reflects displacement of the load centre by 30 km relative to the long-term load. Varying the load half-width and the load centre by ±10 km has only a small impact (<0.5 kPa) on the resolved seasonal stress changes on the faults.

©2014 Macmillan Publishers Limited. All rights reserved